Pre-print submitted version

Tunable Wide-Bandgap Mono-Halide Perovskites.

Yousra El Ajjouri,[a] Ana M. Igual-Muñoz,[a] Michele Sessolo, Francisco Palazon,* and Henk J. Bolink

Instituto de Ciencia Molecular, Universidad de Valencia, C/ Catedrático J. Beltrán 2, 46980 Paterna, Spain

E-mail: francisco.palazon@uv.es
[a] These authors contributed equally

Keywords: perovskites, wide-bandgap, photovoltaics, tin-lead, tandem.

We report herein the mechanochemical synthesis of inorganic as well as hybrid organic-inorganic mono-halide perovskites with tunable bandgaps. We show that the bandgap bowing known for iodide mixed Sn-Pb perovskites is also present in the pure bromide analogous. This results in technologically very interesting materials with bandgaps in the range of 1.7 eV to 1.9 eV. Similar bandgap perovskites are typically achieved by mixing two halides that are prone to segregate over time. This limits the achievable open circuit voltage. For monohalide perovskites this problem is eliminated, making these materials especially promising wide bandgap absorbers for tandem solar cells.

In the last decade, an increasing interest has developed towards halide perovskites as promising materials for optoelectronics and especially photovoltaics (PV). At the time of writing, these materials have already shown to outperform alternative PV technologies, such as copper indium gallium selenide (CIGS) and cadmium telluride (CdTe) solar cells. To date, the world record for perovskite single-junction solar cells has a power conversion efficiency (PCE) of 25.2%.[1] As such, the performance of perovskite-based single-junction solar cells is approaching that of high-efficiency silicon solar cells (PCE = 26.7%). One approach to continue improving the PCE (> 30%) is by the development of multi-junction solar cells.[2–4] A tandem

1

solar cell consists of two different absorbers: a front-cell using a high-bandgap absorber and a back-cell using a low-bandgap material. Thus, photons from different regions of the solar spectrum can be separately harvested by each cell, reducing thermalization losses and hence improving the theoretical maximum PCE of the photovoltaic device. Halide perovskites present a high degree of bandgap tunability based on compositional engineering which makes these materials especially promising for tandem solar cells, based on silicon/perovskite, CIGS/perovskite, or perovskite/perovskite stacks.[5–10] The most used strategy up to now to develop wide-bandgap absorbers consists in mixing different halide anions. Starting from methylammonium lead triiodide (MAPbI$_3$) with a bandgap around 1.55 eV, the controlled substitution of iodide with bromide results in alloyed MAPb(I$_{1-x}$Br$_x$)$_3$ perovskites with bandgaps between 1.57 eV and 2.29 eV.[11–13] Solar cells based on such mixed halide lead-based perovskites have a rather low open circuit voltage. This is generally attributed to phase segregation into separate halide-rich perovskite phases which occurs in particular under illumination..[14] Hence, alternatives to the mixed halide approach for wide bandgap perovskite absorbers are needed. In analogy of previous work on iodide perovskites, [15–20] we substitute part of the divalent lead with divalent tin cations to lower the bandgap of pure bromide analogues.

In detail, we have investigated mixed tin-lead bromide perovskites (ASn$_x$Pb$_{1-x}$Br$_3$) with different A-cations (CH(NH$_2$)$_2^+$ -FA$^+$-, CH$_3$NH$_3^+$ -MA$^+$- and Cs$^+$), and different molar Sn-fractions (0%, 30%, 50%, 70% and 100%). The perovskites CsSn$_x$Pb$_{1-x}$Br$_3$, MASn$_x$Pb$_{1-x}$Br$_3$ and FASn$_x$Pb$_{1-x}$Br$_3$ were prepared by dry mechanochemical synthesis (MCS) via ball-milling of the stoichiometric precursors. This approach enables the formation of perovskites in a time-efficient and solvent-free manner.[21–29] Structural and optical characterization of the mechanochemically-synthesized perovskites were carried out showing good metal mixing and tunable bandgaps. We demonstrate that similar to the iodide Sn-Pb analouges also for the bromide based perovskite the mixed Sn-Pb have bandgaps below the pure Sn or pure Pb based perovskites, an effect known as *bandgap bowing*. This allows us to reach the desired bandgaps (1.7 eV – 1.9 eV) yet with only one halide (bromide) and hence eliminating the

2

posibility of halide segragation. For one of the many prepared perovskites we demonstrate its conversion into thin film absorbers with a bandgap of 1.85 eV using thermal sublimation.

Different perovskites were prepared by neat ball-milling of pristine powder precursors. This mechanochemical approach allows to finely control the stoichiometry of the formed compounds, as it does not rely on solubility. The X-ray diffraction (XRD) patterns of the different perovskites prepared by MCS ($CsSn_xPb_{1-x}Br_3$, $MASn_xPb_{1-x}Br_3$ and $FASn_xPb_{1-x}Br_3$) are presented in **Figure 1**. The grinding of CsBr and $PbBr_2$ leads to the formation of highly-phase pure $CsPbBr_3$ as can be derived from the comparison of the experimental data (black line) and reference bulk pattern (orange histogram) in Figure 1a. This is in agreement with previous reports.[21,30] When increasing amounts of $SnBr_2$ are added as replacement of $PbBr_2$, we do not observe significant changes in the diffraction pattern, except a gradual shift towards higher angles (see Figure S1a for a better visualization). This is ascribed to a shrinkage of the unit cell which is expected as Sn^{2+} has a lower ionic radius than Pb^{2+}. Similar observations can be made for the MA-based perovskites (Figure 1b and Figure S1b). At a first glance it may seem that several experimental peaks do not match with the reference pattern, namely at $2\Theta = 25.2º$, $2\Theta = 37.1º$, and $2\Theta = 48.5º$. However, these reflections are present in the reference pattern and correspond to the (111), (211), and (310) planes. The reason why the relative intensities are different between the experimental data and the reference is unclear, although this is usually ascribed to some degree of preferential crystallographic orientation in the sample. Eventually, we note that for $FAPbBr_3$ no reference pattern exists in the ICSD. Nevertheless, the diffractogram matches that of $MAPbBr_3$ with a shift towards lower angles (Figure 1c and Figure S1c). This suggests that $FAPbBr_3$ is formed and crystallizes in the same space group as $MAPbBr_3$, with a larger unit cell as expected from the larger A-cation. In the case of the $FA(Sn_xPb_{1-x})Br_3$ series, no shift to higher diffraction angles is observed when introducing tin. In fact, the opposite is true for the composition without lead ($FASnBr_3$; Figure S1c). However, it must be noted that this is also accompanied by the emergence of new peaks, most noticeably at $30.6º$. This feature is reminiscent of the vacancy-ordered $A_2Sn(IV)Br_6$ perovskite. Indeed, the main diffraction peak of Cs2SnBr6 is located at $2\theta=30.4º$ (see ICSD reference 434641).

3

This would suggest that Sn(II) is partly oxidized to Sn(IV), which is something that has been already reported by others.[31] It is unclear if this phase was formed during synthesis or upon air exposure, as XRD analysis was necessarily carried out in air. In any case, this phase seems to be absent from all other samples. Thus, we conclude that for high tin-fraction in the mechanochemical synthesis of FA-based bromide perovskites it is less straightforward to obtain phase pure and air stable materials than for the MA and Cs containing ones. For the latter, all materials seem to be air-stable at least for the time of XRD measurements (ca. 1 hour) and under the detection limitations of this technique. In the present work no further stability tests were undertaken.
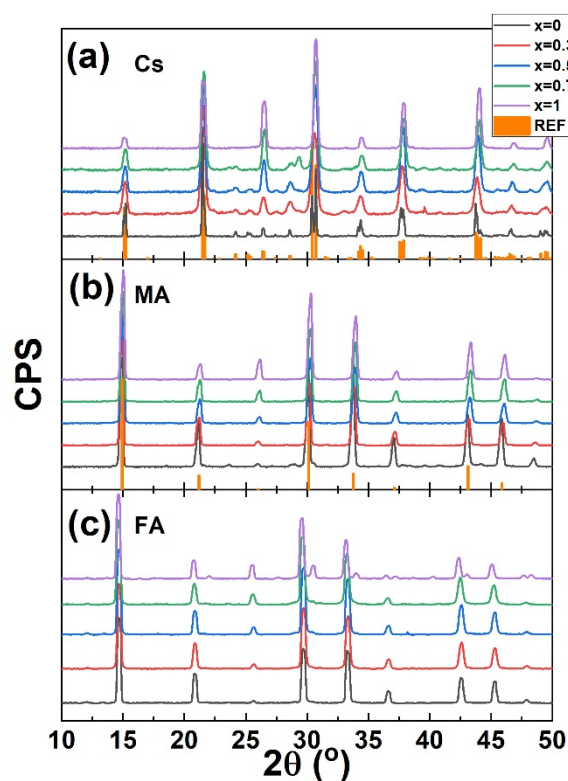
Figure 1. XRD characterization of A(SnxPb1-x)Br3 prepared by MCS. (a) A = Cs, (b) A = MA, (c) A = FA. The molar Sn fraction x is given in legend. Orange histograms correspond to reference bulk patterns for CsPbBr3 (a; ICSD-97851) and MAPbBr3 (b; ICSD-252416) obtained from the inorganic Crystal Structure Database (ICSD).

Figure 2 shows the Tauc plots of all samples (a-c) as derived from the optical absorption spectra as well as bandgap energy values (d) derived from a linear extrapolation of the Tauc plots' onsets. All series (Cs-, MA-, and FA- based mixed tin-lead bromides) show bowing of the bandgap as a function of the tin fraction (Figure 2d). In particular, for FA and MA

perovskites, all mixed tin-lead compositions studied here exhibit a substantially lower bandgap than both pure-tin and pure-lead counterparts. This has been previously observed for iodide perovskites and other semiconductors.[16,32] For bromide perovskites, a similar behaviour has been observed on MA-based single crystals.[33] As explained in the introduction, this is especially relevant for wide-bandgap absorbers in tandem solar cells. For perovskite/perovskite tandem solar cells, a bandgap of around 1.7 eV to 1.9 eV is especially sought after.[34] Based on the data presented in Figure 2d, it appears that FA-based bromide perovskites are to be discarded as these exhibit bandgaps in excess of the desired range. Yet, most MA- and Cs-based mixed tin-lead compositions do exhibit bandgaps in the desired range and therefore may be viable options for front cell perovskite absorbers.
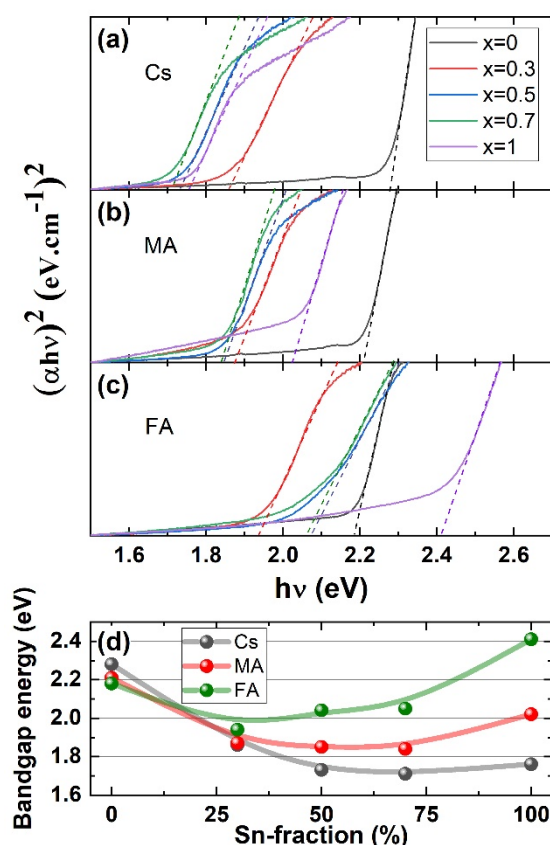
Figure 2. Tauc plots of mixed tin-lead cesium (a), methylammonium (b), and formamidinium (c) bromides, and bandgap energy as a function of tin-fraction as derived from the above plots (d).

It is also worth highlighting that this bandgap-bowing behaviour also holds for mixed A-cation perovskites such as $(MA_{0.5}FA_{0.5})(Sn_xPb_{1-x})Br_3$ prepared as thin films by spin-coating (See Figure S2 in the Supporting Information). Nevertheless, the morphology of such films was found to be very inhomogeneous (see Figure S3). Furthermore, as we highlighted in the introduction, the use of toxic solvents such as DMF in this method hinders the possible upscaling of the approach.

Therefore, we decided to attempt the preparation of thin films by single-source vacuum deposition of the mechanochemically-synthesized powders.[21,35,36] This technique allows for the processing of solid state materials in a simple and fast procedure that does not involve additional solvents or other chemicals. However, to limit possible thermal degradation of the material during the short heating phase, fully-inorganic compounds are preferred. Thus, in view of this and the obtained bandgaps, we attempted to prepare thin films of $CsSn_{0.3}Pb_{0.7}Br_3$. In short, the procedure is as follows: pre-synthesized $CsSn_{0.3}Pb_{0.7}Br_3$ powders are loaded in a molecular evaporation source containing an Al_2O_3 crucible inside a vacuum chamber. After evacuating the pressure to levels around 10^{-6} mbar, the evaporation source is rapidly heated to high temperature. A substrate is placed face down above the evaporation source and a thin film is deposited on it (see experimental section for more details). Subsequently, the film is annealed in nitrogen at 150 ºC for 10 minutes. By adjusting the amount of material placed in the crucible, it is possible to tune the final film thickness. In this way we deposited a 250-nm film (thin) and a 890-nm film (thick), which can be considered of interest for perovskite photovoltaics. It is worth mentioning that films of several hundreds of nanometers cannot be easily obtained by solution processing, due to the constrains in precursors' solubility. X-ray diffraction, absorbance spectra and scanning-electron microscopy images of both films deposited on bare glass substrates are shown in **Figure 3**.
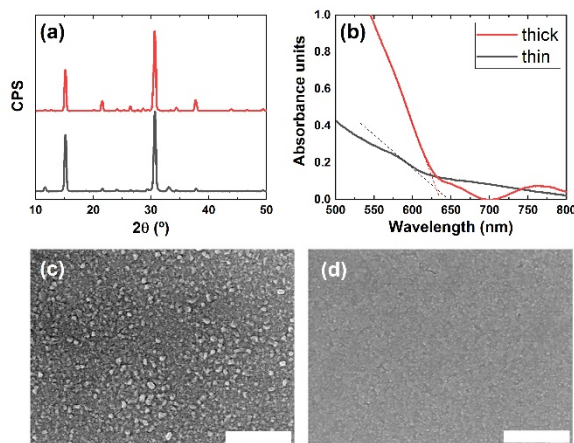
Figure 3. XRD (a), absorbance (b), and SEM (c-d) characterization of a thin film (250 nm; black lines in (a) and (b); SEM image (c)) and a thick film (890-nm; red lines in (a) and (b); SEM image (d)). Scale bars in (c) and (d) represent one micron.

Figure 3a shows a good crystallinity of the Cs(SnPb)Br$_3$ films, with a preferential orientation along the [010] direction as observed from the predominant peaks around 15° and 30° compared to the (non-oriented) powder sample in Figure 1a. Despite an overall good match between the XRD signal of the as-obtained films and the expected pattern for CsMBr$_3$ (M=(Pb$_{1-x}$Sn$_x$), ICSD reference 97851) we note the presence of minor peaks around 11.7º and 12.6º which are a clear indication of M-rich and Cs-rich ternary phases: CsM$_2$X$_5$ and Cs$_4$MX$_6$.[37,38] This is thought to be the result of incongruent melting and phase transformation before evaporation, meaning that a small fraction of the powder material is not sublimed as a single CsMBr$_3$ compound during single-source vacuum deposition (SSVD). Minor differences in crystallinity and morphology between the thin and thick films may be due to heating heterogeneities during the process as a function of material load in the crucible. Indeed, as previously explained, for SSVD all the loaded material is evaporated (contrary to standard co-evaporation process). This means that the loading of the crucible is different for the thin and thick film. As a side-effect this may in turn result in a different heat profile inside the thermal source, which itself changes as the material gets sublimed. These minor inconsistencies may be overcome by a faster sublimation or an optimized post-deposition annealing treatment.

7

The absorbance spectra of both samples (Figure 3b) show an onset around 650 nm, corresponding to a bandgap of 1.9 eV. This is very similar as what was observed for the powders (Figure 2d). We note however that precise determination of this onset is difficult due to the interference fringes that appear in the spectra as a function of film thickness. These fringes do indicate the good optical quality of the films. The films were further analyzed using scanning electron microscopy (SEM). The SEM images show a small-grain texture (<100 nm typical size) without observable pinholes (Figure 3c-d).

We implemented thermally evaporated and solution-processed films of similar composition in single-junction solar cells. However, this mostly resulted in very low and inconsistent performance (see Figure S4), which might be partly due to the poor morphology of the films. For solution-processed films this is obvious from Figure S2. For SSVD-films, we also discussed above the small-grain morphology, which might indicate a considerable amount of amorphous material and high density of defects. It is important to note that during SSVD, powders are rapidly heated to very high temperatures so the evaporation rate is much larger than in standard co-evaporation. This means that evaporated particles (atoms, ions or clusters) have a high kinetic energy that may damage the selective contact layer on which they are deposited. All these hypotheses point to the fact that the low performances of the devices may be due to extrinsic processing parameters and not to the materials themselves. Hence, they might be overcome with further processing optimization.

In summary, the results presented herein demonstrate that it is possible to achieve monohalide wide bandgap perovskites with all three common A-cations (MA, FA, and Cs) as well as mixtures thereof. The obtainable bandgaps, allow for their use as absorber in the front cell of tandem cells with a plurality of low bandgap absorbers, including commercial Si-cells. The use of only bromide cations makes it impossible for halide segregation to occur. The bandgap can be fine-tuned by selecting the proper tin-lead ratio and the use of the either Cs, FA or MA. We also demonstrated that mechanochemically-synthesized perovskite powders can be transferred into high quality thin films using single-source thermal vacuum deposition, maintaining the material's chemical and optical characteristics.

Experimental Section

Materials: Cesium bromide (CsBr, > 99 %), lead(II) bromide (PbBr$_2$, > 98 %) and tin(II) bromide (SnBr$_2$, > 97%) were purchased from TCI. Methylammonium bromide (CH$_6$NBr) and formamidinium bromide (CH$_5$N$_2$Br) were purchased from GreatCell Solar. Tin fluoride (SnF$_2$ 99%) was purchased from Sigma Aldrich. All chemicals were stored in a nitrogen-filled glovebox and used as received without further purification.

Mechanochemical synthesis of AMBr$_3$ powders: Equimolar ABr:MBr$_2$ powders (A=Cs, MA, or FA; M = (Sn$_x$Pb$_{1-x}$) with x = 0, 0.3, 0.5, 0.7, 1) were mixed inside a nitrogen-filled glovebox. Then, approximately 3 grams of the mixed precursors powders was introduced inside 10 mL zirconia ball-mill jars with 2 zirconia beads of 10 mm in diameter. The jars were closed under nitrogen so that the powders were not exposed to air. Then ball-milling was performed with a MM-400 straight ball-mill from Retsch, at a frequency of 30 Hz for 2 hours.

Single-source vacuum deposition: Pre-synthesized Cs(Sn$_{0.3}$Pb$_{0.7}$)Br$_3$ perovskite powders were converted in thin-films by means of a single-source vacuum deposition. Perovskite thin films were deposited in a vacuum chamber (Vaksis R&D and Engineering) at 10^{-6} mbar, equipped with temperature controlled alumina thermal sources (Creaphys GmbH) and quartz crystal microbalance thickness sensors. Mechanical shutters both at the thermal source and at the substrate holder were used to control the deposition process.

Solution-processed thin films: MABr, FABr, PbBr$_2$ and SnBr$_2$ were individually dissolved in a mixture of DMF and DMSO (85/15 v/v), at a concentration of 1.1M. For SnBr$_2$ solutions, 20% mol SnF$_2$ was added. MAPbBr$_3$ and FASnBr$_3$ solutions were prepared in two separate vials and stirred overnight. Prior to spin coating, the solutions were mixed to lead the desired stoichiometry (MA$_{0.5}$FA$_{0.5}$Sn$_{0.5}$Pb$_{0.5}$Br$_3$). The solution was then filtered with a PTFE (0.22µm)

9

filter and spin-coated on the substrate at 2500 rpm for 45 seconds. After 10 seconds of spin-coating, 100 µL toluene was drop-casted as antisolvent. The transparent films quickly turned to their final color as shown in Fig. S2. An annealing at 100 ºC for 10 minutes was carried out after spin-coating.

Device preparation:

Glass substrates with a patterned indium tin oxide transparent electrode were rinsed with detergent, water, Millipore water and isopropanol during 5 minutes with sonication for each step. Then, they were transferred to a UV-Ozone chamber and activated for 20 minutes. After cleaning, PEDOT:PSS (Clevios PVP CH8000 from Heraeus) was spin-coated on the substrates at 3000 rpm for 60 s and annealed at 150 ºC during 15 minutes. The substrates were transferred to an N_2-filled glovebox and the $MA_{0.5}FA_{0.5}Sn_{0.5}Pb_{0.5}Br_3$ layer was spin-coated on them as described previously. Afterwards, a solution containing of indene-C_{60}-propionic acid hexyl ester (IPH, 20 mg mL^{-1}) in chlorobenzene was deposited by spin-coating at 1400 rpm for 50 s. Finally, the metal contacts (10 nm Ba capped with 100 nm Ag) were thermally evaporated at a pressure of $3·10^{-6}$ mbar.

XRD characterization: X-ray diffraction was measured with a Panalytical Empyrean diffractometer equipped with CuKα anode operated at 45 kV and 30 mA and a Pixel 1D detector in scanning line mode. Single scans were acquired in the 2θ= 10° to 50° range in Bragg-Brentano geometry in air. Data analysis was performed with HighScore Plus software.

Optical absorption characterization: Absorbance was measured with a High Power UV-VIS fiber light source, integrated sphere and Avantes Starline AVASpec-2048L spectrometer in reflection mode.

Scanning Electron Microscopy: Electron microscopy characterization was performed using a Hitachi S-4800 microscope operating at an accelerating voltage of 10 kV.

Acknowledgements

References

[1]   NREL, Best Research-Cell Efficiency Chart., https://www.nrel.gov/pv/cell-
        efficiency.html, accessed: Aug., 2019.

[2]   A. De Vos, *J. Phys. D. Appl. Phys.* **1980**, *13*, 839.

[3]   W. Shockley, H. J. Queisser, *J. Appl. Phys.* **1961**, *32*, 510.

[4]   D. P. McMeekin, G. Sadoughi, W. Rehman, G. E. Eperon, M. Saliba, M. T. Hörantner,
        A. Haghighirad, N. Sakai, L. Korte, B. Rech, M. B. Johnston, L. M. Herz, H. J. Snaith,
        Science (80-.). **2016**, *351*, 151.

[5]   D. Forgàcs, L. Gil-Escrig, D. Pérez-Del-Rey, C. Momblona, J. Werner, B. Niesen, C.
        Ballif, M. Sessolo, H. J. Bolink, *Adv. Energy Mater.* **2017**, *7*, 1.

[6]   E. Köhnen, M. Jošt, A. B. Morales-Vilches, P. Tockhorn, A. Al-Ashouri, B. Macco, L.
        Kegelmann, L. Korte, B. Rech, R. Schlatmann, B. Stannowski, S. Albrecht, *Sustain.
        Energy Fuels* **2019**, *3*, 1995.

[7]   L. L. Yan, C. Han, B. Shi, Y. Zhao, X. D. Zhang, *Mater. Today Nano* **2019**, *7*, 100045.

[8]   A. Guchhait, H. A. Dewi, S. W. Leow, H. Wang, G. Han, F. Bin Suhaimi, S. Mhaisalkar,
        L. H. Wong, N. Mathews, *ACS Energy Lett.* **2017**, *2*, 807.

[9]   P. Mantilla-Perez, T. Feurer, J. P. Correa-Baena, Q. Liu, S. Colodrero, J. Toudert, M.
        Saliba, S. Buecheler, A. Hagfeldt, A. N. Tiwari, J. Martorell, *ACS Photonics* **2017**, *4*,
        861.

[10]   G. E. Eperon, G. E. Eperon, T. Leijtens, K. A. Bush, R. Prasanna, T. Green, J. T.
        Wang, D. P. Mcmeekin, G. Volonakis, R. L. Milot, R. May, A. Palmstrom, J. Daniel, R.
        A. Belisle, J. B. Patel, E. S. Parrott, R. J. Sutton, W. Ma, B. Conings, A. Babayigit, H.
        Boyen, S. Bent, F. Giustino, M. Herz, M. B. Johnston, M. D. Mcgehee, H. J. Snaith,
        2016, *9717*, 1.

[11]   J. H. Noh, S. H. Im, J. H. Heo, T. N. Mandal, S. Il Seok, *Nano Lett.* **2013**, *13*,
        1764−1769.

[12]   Y. Zhao, K. Zhu, *J. Am. Chem. Soc.* **2014**, *136*, 12241.

[13] C. Bi, Y. Yuan, Y. Fang, J. Huang, *Adv. Energy Mater.* **2015**, *5*, 1.

[14] E. L. Unger, L. Kegelmann, K. Suchan, D. Sörell, L. Korte, S. Albrecht, *J. Mater. Chem. A* **2017**, *5*, 11401.

[15] D. Zhao, Y. Yu, C. Wang, W. Liao, N. Shrestha, C. R. Grice, A. J. Cimaroli, L. Guan, R. J. Ellingson, K. Zhu, X. Zhao, R. G. Xiong, Y. Yan, *Nat. Energy* **2017**, *2*, 1.

[16] Z. Yang, A. Rajagopal, S. B. Jo, C. C. Chueh, S. Williams, C. C. Huang, J. K. Katahara, H. W. Hillhouse, A. K. Y. Jen, *Nano Lett.* **2016**, *16*, 7739.

[17] F. Hao, C. C. Stoumpos, R. P. H. Chang, M. G. Kanatzidis, *J. Am. Chem. Soc.* **2014**, *136*, 8094.

[18] W. Liao, D. Zhao, Y. Yu, N. Shrestha, K. Ghimire, C. R. Grice, C. Wang, Y. Xiao, A. J. Cimaroli, R. J. Ellingson, N. J. Podraza, K. Zhu, R. G. Xiong, Y. Yan, *J. Am. Chem. Soc.* **2016**, *138*, 12360.

[19] J. Im, C. C. Stoumpos, H. Jin, A. J. Freeman, M. G. Kanatzidis, *J. Phys. Chem. Lett.* **2015**, *6*, 3503.

[20] C. C. Stoumpos, C. D. Malliakas, M. G. Kanatzidis, *Inorg. Chem.* **2013**, *52*, 9019.

[21] Y. El Ajjouri, F. Palazon, M. Sessolo, H. J. Bolink, *Chem. Mater.* **2018**, *30*, 7423.

[22] Y. El Ajjouri, V. S. Chirvony, N. Vassilyeva, M. Sessolo, F. Palazon, H. J. Bolink, *J. Mater. Chem. C* **2019**, *7*, 6236.

[23] Y. El Ajjouri, V. S. Chirvony, M. Sessolo, F. Palazon, H. J. Bolink, *RSC Adv.* **2018**, *8*, 41548.

[24] Y. El Ajjouri, F. Locardi, M. C. Gélvez-Rueda, M. Prato, M. Sessolo, M. Ferretti, F. C. Grozema, F. Palazon, H. J. Bolink, *Energy Technol.* **2019**, *1900788*, ente. 201900788.

[25] F. Palazon, Y. El Ajjouri, H. J. Bolink, *Adv. Energy Mater.* **2019**, *1902499*, 1.

[26] L. Protesescu, S. Yakunin, O. Nazarenko, D. N. Dirin, M. V. Kovalenko, *ACS Appl. Nano Mater.* **2018**, *1*, 1300.

[27] A. D. Jodlowski, A. Yépez, R. Luque, L. Camacho, G. de Miguel, *Angew. Chemie - Int. Ed.* **2016**, *55*, 14972.

[28] D. Prochowicz, M. Saski, P. Yadav, M. Grätzel, J. Lewiński, *Acc. Chem. Res.* **2019**,

52, 3233.

[29]   D. Prochowicz, M. Franckevičius, A. M. Cieślak, S. M. Zakeeruddin, M. Grätzel, J. Lewiński, F. Franckevičius, A. M. Cié, S. M. Zakeeruddin, M. Grätzelgrätzel, J. Lewí, *J. Mater. Chem. A* **2015**, *3*, 20772.

[30]   F. Palazon, Y. El Ajjouri, P. Sebastia-Luna, S. Lauciello, L. Manna, H. J. Bolink, *J. Mater. Chem. C* **2019**, *7*, 11406.

[31]   X. Qiu, B. Cao, S. Yuan, X. Chen, Z. Qiu, Y. Jiang, Q. Ye, H. Wang, H. Zeng, J. Liu, M. G. Kanatzidis, *Sol. Energy Mater. Sol. Cells* **2017**, *159*, 227.

[32]   A. Goyal, S. McKechnie, D. Pashov, W. Tumas, M. Van Schilfgaarde, V. Stevanović, *Chem. Mater.* **2018**, *30*, 3920.

[33]   D. Ju, Y. Dang, Z. Zhu, H. Liu, C. C. Chueh, X. Li, L. Wang, X. Hu, A. K. Y. Jen, X. Tao, *Chem. Mater.* **2018**, *30*, 1556.

[34]   T. Leijtens, K. A. Bush, R. Prasanna, M. D. McGehee, *Nat. Energy* **2018**, *3*, 828.

[35]   P. Sebastia-Luna, J. Navarro-Alapont, M. Sessolo, F. Palazon, H. J. Bolink, *Chem. Mater.* **2019**, *31*, 10205.

[36]   M. J. Crane, D. M. Kroupa, J. Y. Roh, R. T. Anderson, M. D. Smith, D. R. Gamelin, *ACS Appl. Energy Mater.* **2019**, *2*, 4560.

[37]   F. Palazon, C. Urso, L. De Trizio, Q. Akkerman, S. Marras, F. Locardi, I. Nelli, M. Ferretti, M. Prato, L. Manna, *ACS Energy Lett.* **2017**, 2445.

[38]   F. Palazon, S. Dogan, S. Marras, F. Locardi, I. Nelli, P. Rastogi, M. Ferretti, M. Prato, R. Krahne, L. Manna, *J. Phys. Chem. C* **2017**, *121*, 11956.
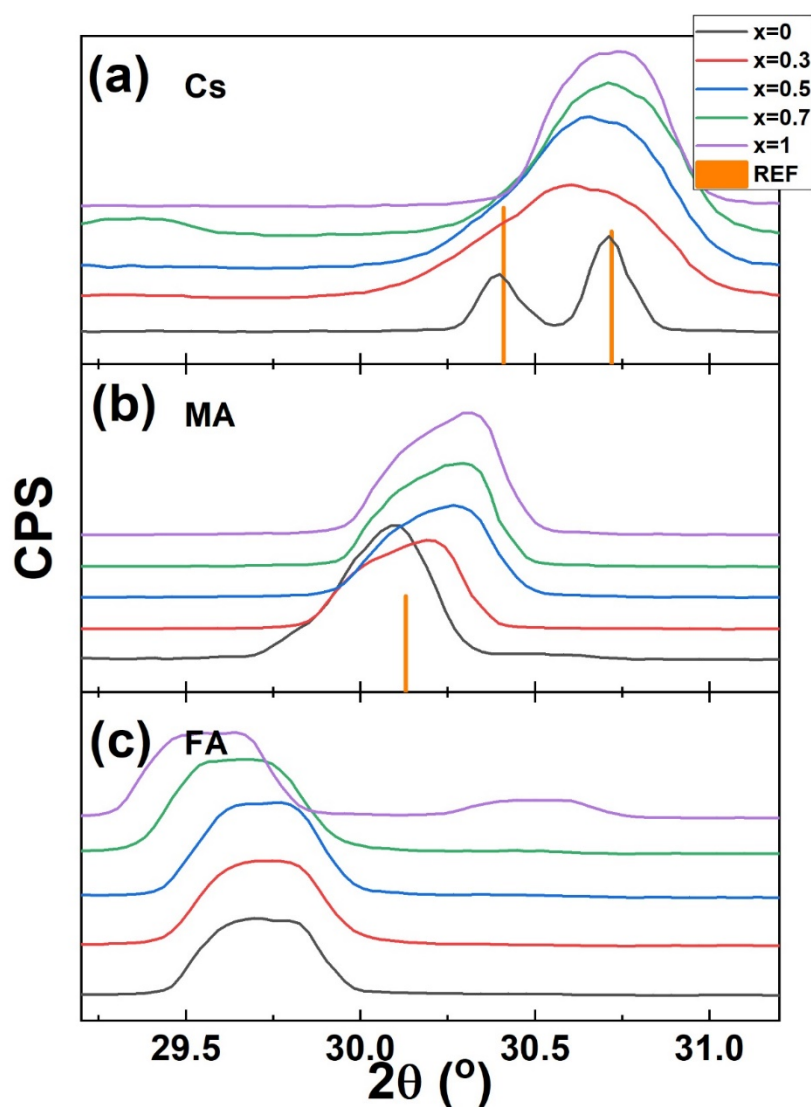
Supporting Information

Tunable Wide-Bandgap Mono-Halide Perovskites.

*Yousra El Ajjouri, Ana M. Igual-Muñoz, Michele Sessolo, Francisco Palazon,* and Henk J. Bolink*

Instituto de Ciencia Molecular, Universidad de Valencia, C/ Catedrático J. Beltrán 2, 46980 Paterna, Spain

E-mail: francisco.palazon@uv.es

Keywords: perovskites, wide-bandgap, photovoltaics, tin-lead, tandem.

Figure S 1. XRD of mechanochemically-synthesized compounds in the 2 theta = 29.2º to 31.2º range ("zoom" from Figure 1). Bigger A-cations shift diffractions peak to lower angles (larger interatomic distances). Smaller B-cations (increasing amount of Sn) shift diffraction peaks to higher angles (lower interatomic distances) except in the FA-series. Comments in the main manuscript.
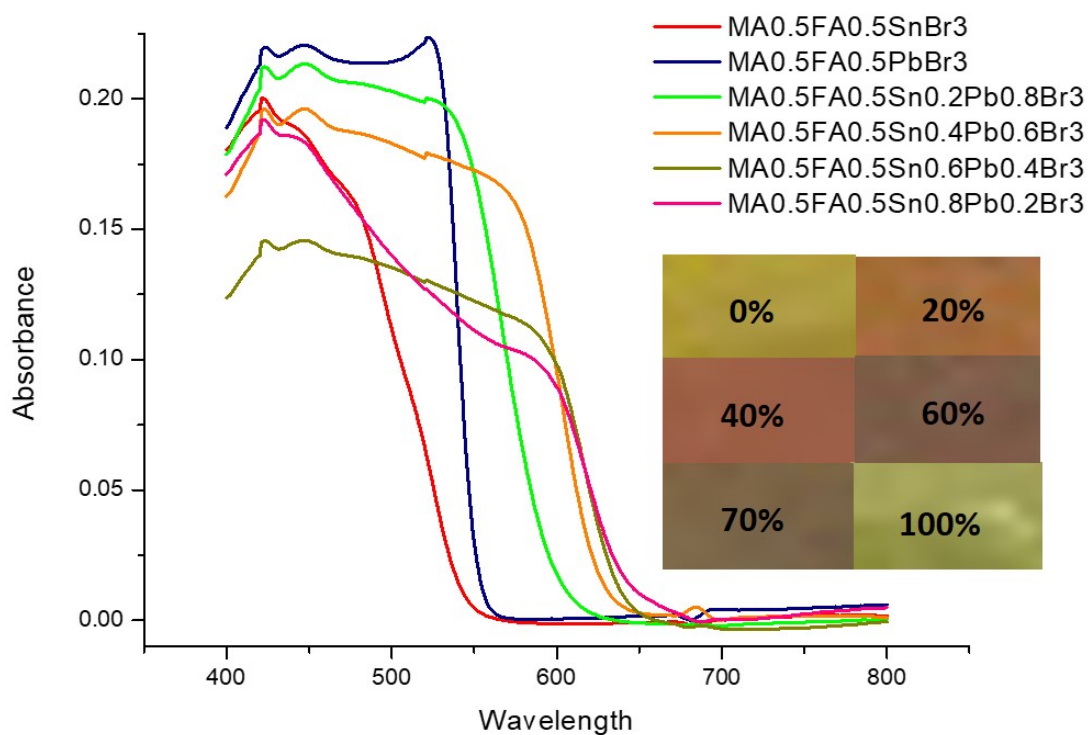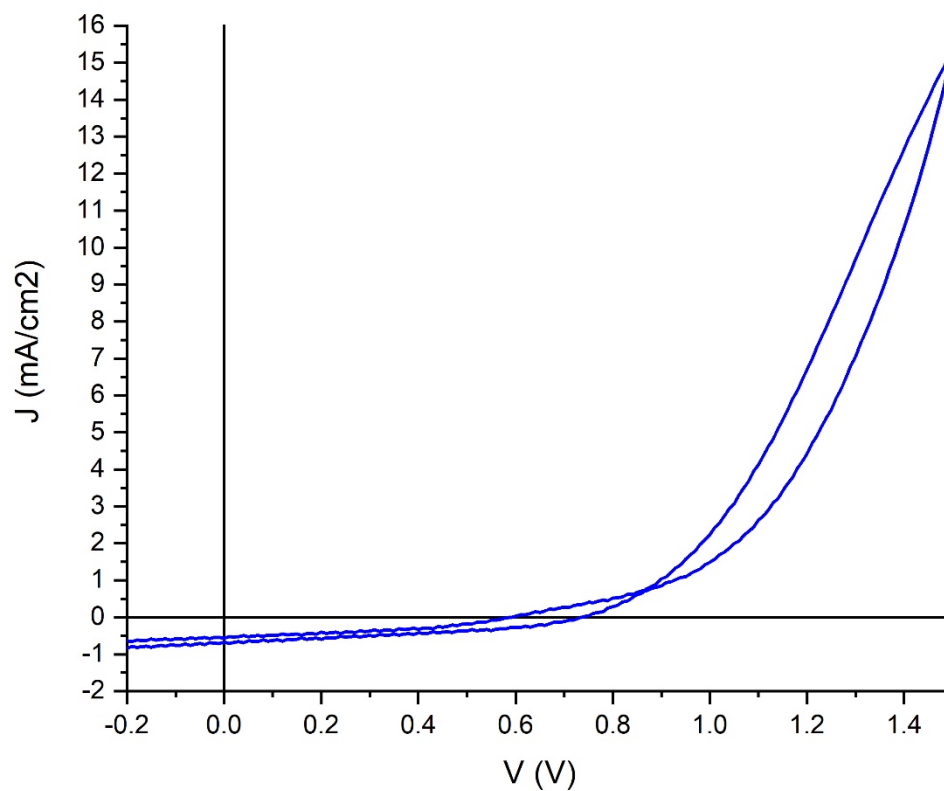
Figure S 2. Absorption spectra and photographs of solution-processed thin films of $(MA_{0.5}FA_{0.5})(Sn_xPb_{1-x})Br_3$ thin films showing bandgap bowing.
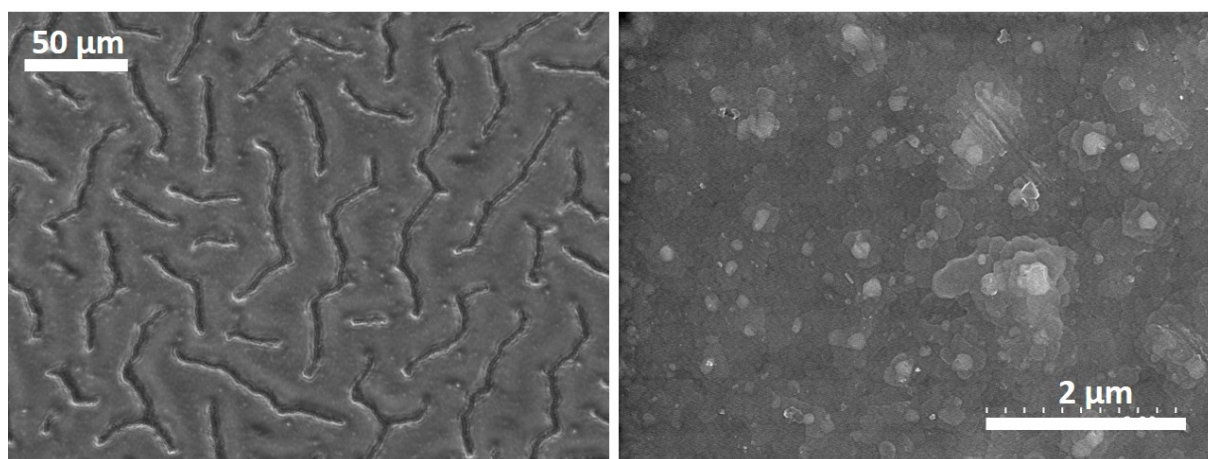
Figure S 3. SEM of solution-processed thin films showing important heterogeneity.

Figure S 4. Current density vs voltage curve of solar cell based on solution-processed $MA_{0.5}Pb_{0.5}(Sn_{0.5}Pb_{0.5})Br_3$ film showing poor photovoltaic performance (PCE < 1%) and considerable hysteresis.